

Quasi-static thermoelastic deformation in an elastic half-space: theory and application to InSAR observations at Izu-Oshima volcano, Japan

M. Furuya^{1,2}

¹Earthquake Research Institute, University of Tokyo, Tokyo 113-0032, Japan. E-mail: furuya@eri.u-tokyo.ac.jp

²CIRES and Department of Physics, University of Colorado at Boulder, CO 80303–390, USA

Accepted 2005 February 8. Received 2005 January 11; in original form 2004 September 1

SUMMARY

We derive closed analytical solutions for quasi-static thermoelastic deformation in response to instantaneous point and spherical heat sources in an elastic half-space. Since we can take advantage of the solutions for an infinite medium, the derivation of solutions for a semi-infinite medium is straightforward. We examine the spatial and temporal evolution of thermoelastic deformation for point and spherical heat sources. We applied the solution to a radar interferometric observation of post-eruptive deformation associated with the 1986 fissure eruption at Izu-Oshima volcano, Japan. Assuming a spherical heat source at a depth of 240 m with a volume of $1.15 \times 10^7 \text{ m}^3$ and a temperature step 10^3 K , the predicted rate of post-eruptive ground movement agrees with the observed rate within observational errors. Also, the same parameter values allow us to compute the co-eruptive ground displacement by the effect of mass intrusion, whose amplitude is consistent with the observed height (45 m) of the newly formed cone. The derived solutions can be applied to transient ground displacements observed at active volcanoes, and allow us to evaluate the heat amount of magma intruded at very shallow depths.

Key words: deformation, geodesy, thermoelasticity, volcanology.

1 INTRODUCTION

Interruptive and co-eruptive ground displacements at active volcanoes offer important information about what is going on beneath the surface. They have commonly been interpreted in terms of the so-called Mogi model (Mogi 1958). This is an inflative or deflative mechanical point source in an elastic half-space, and is supposed to represent an injection or ejection of magma into or out of the chamber. In the meantime, because of marked improvements in space geodetic techniques such as the Global Positioning System and satellite radar interferometry, recent measurements of ground displacement have revealed significant post-eruptive deformation at a number of active volcanoes around the world. It is easy to qualitatively interpret those observations as due to thermoelastic contraction. However, quantitative modelling of post-eruptive deformation in previous studies has relied upon numerical techniques such as the finite-element method (e.g. Briole *et al.* 1997; Stevens *et al.* 2001), since no simple analytical models have been available. The Mogi source only accounts for mass intrusion, and it does not consider a transient thermoelastic effect associated with the intruded magma.

Furuya (2004) gave a closed analytical solution for a quasi-static thermoelastic deformation in response to an instantaneous point heat source, and applied it to the post-eruptive deformation at Miyakejima volcano (Japan) observed by interferometric synthetic aperture radar (InSAR). The first purpose of this paper is to extend the point source solution to spherical shell and spherical volume heat sources, and to compare the spatiotemporal behaviour of these sources. Closed analytical solutions for spherical sources in an infinite region are shown, and we will describe a recipe for computing a quasi-static thermoelastic response in an elastic half-space due to an instantaneous heat source. The second purpose is to apply the derived formulation to the post-eruptive deformation at Izu-Oshima volcano (Japan) observed by InSAR, and compare the observations with the prediction.

2 THEORY

The thermoelastic response due to a non-isothermal temperature distribution has been of practical importance in a wide range of disciplines (e.g. Nowacki 1962). In the geoscience literature the static solution has been applied to some geothermal fields and volcanoes (Fialko & Simons 2000; Masterlark & Lu 2004). However, the static solution cannot explicitly take into account the effect of spatiotemporal evolution

in temperature associated with thermal diffusion upon the displacement field. A closed analytical solution for the quasi-static thermoelastic deformation due to an instantaneous point heat source can be easily derived in an infinite space (Nowacki 1962, p. 200) (see also Wang 2000, p. 110); the poroelasticity theory has many mathematical analogies with the thermoelasticity theory, but we do not go into the details in this paper. Nevertheless, in the former literature covering both thermoelasticity (Nowacki 1962, chapter III) and poroelasticity (Wang 2000, chapter 9) it has been rather complicated to derive the corresponding solution for a semi-infinite space. As a probable consequence, there has been no application of closed analytical solutions for the quasi-static thermoelastic response to geophysical problems, with the exception of the paper by Furuya (2004).

Meanwhile, Davies (2003) recently showed that the classical solutions by Mindlin & Cheng (1950a,b) for the thermoelastic response in an elastic half-space medium can be derived in a straightforward way, taking advantage of the solution for an infinite region. Actually, the result of Davies (2003) can even be extended to a quasi-static solution in which temperature variation over time is taken into account (Davies 2003, personal communication). By ‘quasi-static,’ we mean that the acceleration term in the momentum balance equation can be neglected, and that the heat generated from the deformed media is also neglected in the thermal equation. Thereby, time enters the elastic equation only as a parameter, and the derivation of a ‘quasi-static’ solution is greatly simplified. Following the central result in Davies (2003), a half-space solution for the quasi-static response can be derived from

$$\mathbf{u}(\mathbf{x}, t) = \mathbf{u}^{(\infty)} + (3 - 4\nu)\bar{\mathbf{u}}^{(\infty)} - 2x_3 \left(\bar{\epsilon}_{13}^{(\infty)}, \bar{\epsilon}_{23}^{(\infty)}, -\bar{\epsilon}_{33}^{(\infty)} \right), \quad (1)$$

where \mathbf{u} and ϵ_{ij} are displacement and strain, respectively, the superscript (∞) stands for the solution in an infinite space, and the quantities with the over bars, $\bar{\mathbf{u}}^{(\infty)}$ and $\bar{\epsilon}_{ij}^{(\infty)}$, are derived by simply replacing x_3 in the corresponding infinite solution with $-x_3$. That is, $\bar{\mathbf{u}}^{(\infty)}(x_1, x_2, x_3, t) = \mathbf{u}^{(\infty)}(x_1, x_2, -x_3, t)$, and $\bar{\epsilon}^{(\infty)}(x_1, x_2, x_3, t) = \epsilon^{(\infty)}(x_1, x_2, -x_3, t)$. Bold type is used to represent a vector consisting of three components. Namely, once a solution for an infinite space is known, one can immediately and readily obtain the corresponding solution for a semi-infinite space. In the following subsections we will derive solutions in an infinite space which can be used to derive half-space solutions.

2.1 An instantaneous point heat source

The quasi-static displacement potential for infinite space, $\phi^{(\infty)}(\mathbf{x}, t)$, due to an instantaneous heat source of unit intensity $q(\mathbf{x}, t) = \delta(t)\delta(R)$ at (ξ_1, ξ_2, ξ_3) is known as (Nowacki 1962)

$$\phi^{(\infty)}(\mathbf{x}, t) = -\frac{m}{4\pi R} \operatorname{erf}\left(\frac{R}{\sqrt{\theta}}\right), \quad (2)$$

where

$$R \equiv \sqrt{(x_1 - \xi_1)^2 + (x_2 - \xi_2)^2 + (x_3 - \xi_3)^2}, \quad (3)$$

$$m \equiv \frac{\alpha(1 + \nu)}{1 - \nu}, \quad (4)$$

$$\theta \equiv 4\kappa t. \quad (5)$$

The $\operatorname{erf}(x)$ is the error function (Abramowitz & Stegun 1972), and α , ν and κ are the linear thermal expansion coefficient, Poisson’s ratio and thermal diffusivity, respectively. The dimension of $q(\mathbf{x}, t)$ is not [J] but $[\text{m}^3 \text{K}]$, since it is normalized by a product of density and heat capacity, ρc . The infinity solution $u_i^{(\infty)}(\mathbf{x}, t)$ ($i = 1, 2, 3$) is found to be

$$u_i^{(\infty)}(\mathbf{x}, t) = \phi_i^{(\infty)} = \frac{m}{4\pi} \left(\frac{x_i - \xi_i}{R^3} \right) \left[\operatorname{erf}\left(\frac{R}{\sqrt{\theta}}\right) - \frac{2R}{\sqrt{\pi\theta}} \exp\left(-\frac{R^2}{\theta}\right) \right]. \quad (6)$$

To derive solutions for a half-space, the strains for infinite medium below are necessary (see eq. 1):

$$\epsilon_{ii}^{(\infty)} = \frac{m}{4\pi R^3} \left(1 - \frac{3(x_i - \xi_i)^2}{R^2} \right) \left[\operatorname{erf}\left(\frac{R}{\sqrt{\theta}}\right) - \frac{2R}{\sqrt{\pi\theta}} \exp\left(-\frac{R^2}{\theta}\right) \right] + \frac{4}{R^2} \frac{(x_i - \xi_i)^2}{\sqrt{\pi\theta^{3/2}}} \exp\left(-\frac{R^2}{\theta}\right), \quad (7)$$

$$\epsilon_{ij}^{(\infty)} = \frac{3m(x_i - \xi_i)(x_j - \xi_j)}{4\pi R^5} \left[\frac{2R}{\sqrt{\pi\theta}} \left(1 + \frac{2R^2}{3\theta} \right) \exp\left(-\frac{R^2}{\theta}\right) - \operatorname{erf}\left(\frac{R}{\sqrt{\theta}}\right) \right] \quad (i \neq j). \quad (8)$$

2.2 A heat source on a spherical surface

Taking advantage of the potential eq. (2) due to a point heat source, we will derive the deformation potential due to a heat source over a spherical surface with radius of a (Fig. 1). Supposing that the surface density of the heat source is η , we can derive the potential $\Phi_{\text{ss}}^{(\infty)}$ at the point P (Fig. 1) by

$$\begin{aligned} \Phi_{\text{ss}}^{(\infty)} &= -\frac{m}{4\pi} \int \int \frac{\eta a \sin \psi d\lambda d\psi}{\sqrt{R^2 + a^2 - 2Ra \cos \psi}} \operatorname{erf}\left(\frac{\sqrt{R^2 + a^2 - 2Ra \cos \psi}}{\sqrt{\theta}}\right), \\ &= -\frac{\eta a m \sqrt{\theta}}{2R} \left[X + \operatorname{ierfc}(X) \right]_{|R-a|/\sqrt{\theta}}^{(R+a)/\sqrt{\theta}}, \end{aligned} \quad (9)$$

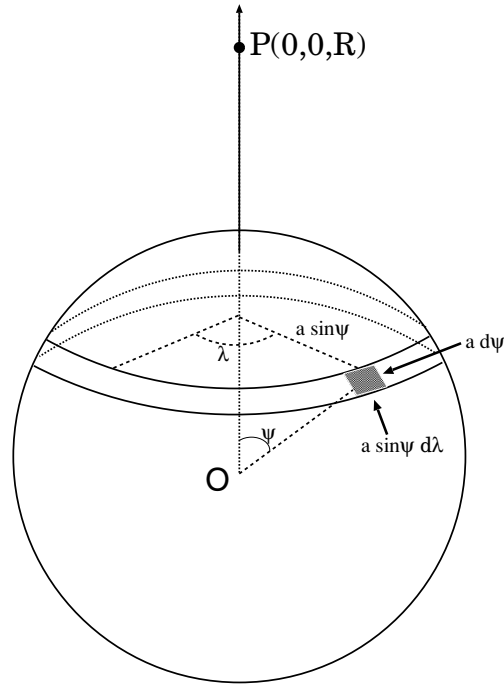


Figure 1. The heat source is distributed on a spherical surface of radius a with surface density η . Upon integrating the heat source element over the spherical surface, we can derive the displacement potential: see eq. (9).

where $\text{ierfc}(X)$ is the integral of the error function (Abramowitz & Stegun 1972), and $[f(X)]_{X_0}^{X_1} = f(X_1) - f(X_0)$: a detailed derivation is shown in Appendix A.

For the case of $R > a$, the first and second derivatives of $\Phi_{ss}^{(\infty)}$ with respect to R are:

$$\Phi_{ss,R}^{(\infty)} = \frac{\eta a^2 m}{R^2} \left(1 + \frac{\sqrt{\theta}}{2a} \left[\text{ierfc}(X) + \frac{R}{\sqrt{\theta}} \text{erfc}(X) \right]_{(R-a)/\sqrt{\theta}}^{(R+a)/\sqrt{\theta}} \right), \quad (10)$$

$$\Phi_{ss,RR}^{(\infty)} = -\frac{2\eta a^2 m}{R^3} \left(1 + \frac{\sqrt{\theta}}{2a} \left[\text{ierfc}(X) + \frac{R}{\sqrt{\theta}} \text{erfc}(X) + \frac{R}{\sqrt{\pi\theta^{3/2}}} \exp(-X^2) \right]_{(R-a)/\sqrt{\theta}}^{(R+a)/\sqrt{\theta}} \right). \quad (11)$$

Corresponding solutions for displacement $u_i^{(\infty)}(\mathbf{x}, t)$, strains $\epsilon_{ii}^{(\infty)}$ and $\epsilon_{ij}^{(\infty)}$ ($i, j = 1, 2, 3$) are found to be

$$u_i^{(\infty)} = \frac{x_i - \xi_i}{R} \Phi_{ss,R}^{(\infty)}, \quad (12)$$

$$\epsilon_{ii}^{(\infty)} = \frac{1}{R} \left[1 - \left(\frac{x_i - \xi_i}{R} \right)^2 \right] \Phi_{ss,R}^{(\infty)} + \left(\frac{x_i - \xi_i}{R} \right)^2 \Phi_{ss,RR}^{(\infty)}, \quad (13)$$

$$\epsilon_{ij}^{(\infty)} = \frac{(x_i - \xi_i)(x_j - \xi_j)}{R^2} \left(\Phi_{ss,RR}^{(\infty)} + \frac{1}{R} \Phi_{ss,R}^{(\infty)} \right), \quad (i \neq j). \quad (14)$$

The relation between total heat Q and heat source surface density η is $Q = 4\pi a^2 \eta$.

2.3 A heat source in a spherical volume

We can derive a deformation potential $\Phi_{sv}^{(\infty)}$ due to a heat source in a spherical volume of radius r , by integrating the spherical surface potential (eq. (9)) from 0 to r with respect to a . For a later application, we consider the case of $R > r$; the derivation for the case of $R < r$ can be similarly done:

$$\begin{aligned} \Phi_{sv}^{(\infty)} &= \int_0^r \Phi_{ss}^{(\infty)}(a) da, \\ &= -\int_0^r \frac{\sigma a^2 m}{R^2} da - \frac{\sigma m \sqrt{\theta}}{2R} \int_0^r \left[a \text{ierfc}\left(\frac{R+a}{\sqrt{\theta}}\right) - a \text{ierfc}\left(\frac{R-a}{\sqrt{\theta}}\right) \right] da, \\ &= -\frac{\sigma m r^3}{3R} - \frac{\sigma m \theta^{3/2}}{2R} \left[\frac{R}{\sqrt{\theta}} i^2 \text{erfc}(X) + \frac{X^2}{2} \text{ierfc}(X) + \frac{X^3}{6} \text{erfc}(X) - \frac{\exp(-X^2)}{6\sqrt{\pi}} (X^2 + 1) \right]_{(R-r)/\sqrt{\theta}}^{(R+r)/\sqrt{\theta}}, \end{aligned} \quad (15)$$

where $i^2 \operatorname{erfc}(X)$ is the integral of $\operatorname{ierfc}(X)$ (Carslaw & Jaeger 1959). The necessary integration formula is shown in Appendix B. The relation between total heat Q and heat source volume density σ is $Q = (4/3)\pi a^3 \sigma$.

The first and second derivatives of $\Phi_{sv}^{(\infty)}$ with respect to R are:

$$\Phi_{sv,R}^{(\infty)} = \frac{\sigma m r^3}{3R^2} + \frac{\sigma m \theta^{3/2}}{2R^2} \left[\left(\frac{X^2}{2} - \frac{RX}{\sqrt{\theta}} + \frac{R^2}{\theta} \right) \operatorname{ierfc}(X) + \frac{X^3}{6} \operatorname{erfc}(X) - \frac{\exp(-X^2)}{6\sqrt{\pi}} (X^2 + 1) \right]_{\frac{(R-r)/\sqrt{\theta}}{(R+r)/\sqrt{\theta}}}, \quad (16)$$

$$\Phi_{sv,RR}^{(\infty)} = -\frac{2\sigma m r^3}{3R^3} - \frac{\sigma m \theta^{3/2}}{R^3} \left[\frac{1}{2} \left(X - \frac{R}{\sqrt{\theta}} \right)^2 \operatorname{ierfc}(X) + \left(\frac{X^3}{6} - \frac{R^2 X}{2\theta} + \frac{R^3}{2\theta^{3/2}} \right) \operatorname{erfc}(X) - \frac{\exp(-X^2)}{6\sqrt{\pi}} (X^2 + 1) \right]_{\frac{(R-r)/\sqrt{\theta}}{(R+r)/\sqrt{\theta}}}. \quad (17)$$

Corresponding solutions for both displacement and strain can be derived in the same manner as eqs (12)–(14), using eqs (15)–(17).

3 SOLUTION IN A HALF-SPACE: NUMERICAL RESULTS

Substituting the solutions for infinite space into eq. (1), we can derive the corresponding solutions for semi-infinite space. We will show numerical results, and interpret the spatial and temporal evolution of thermoelastic deformation in response to an instantaneous heat source.

3.1 Point source

Figs 2(a)–(i) show a snapshot of the temporal evolution of displacement fields in the vertical cross-section passing through a point heat source at a depth of 50 m; all the displacement vectors are scaled to the same length, and are referred to the original state. The heat magnitude of

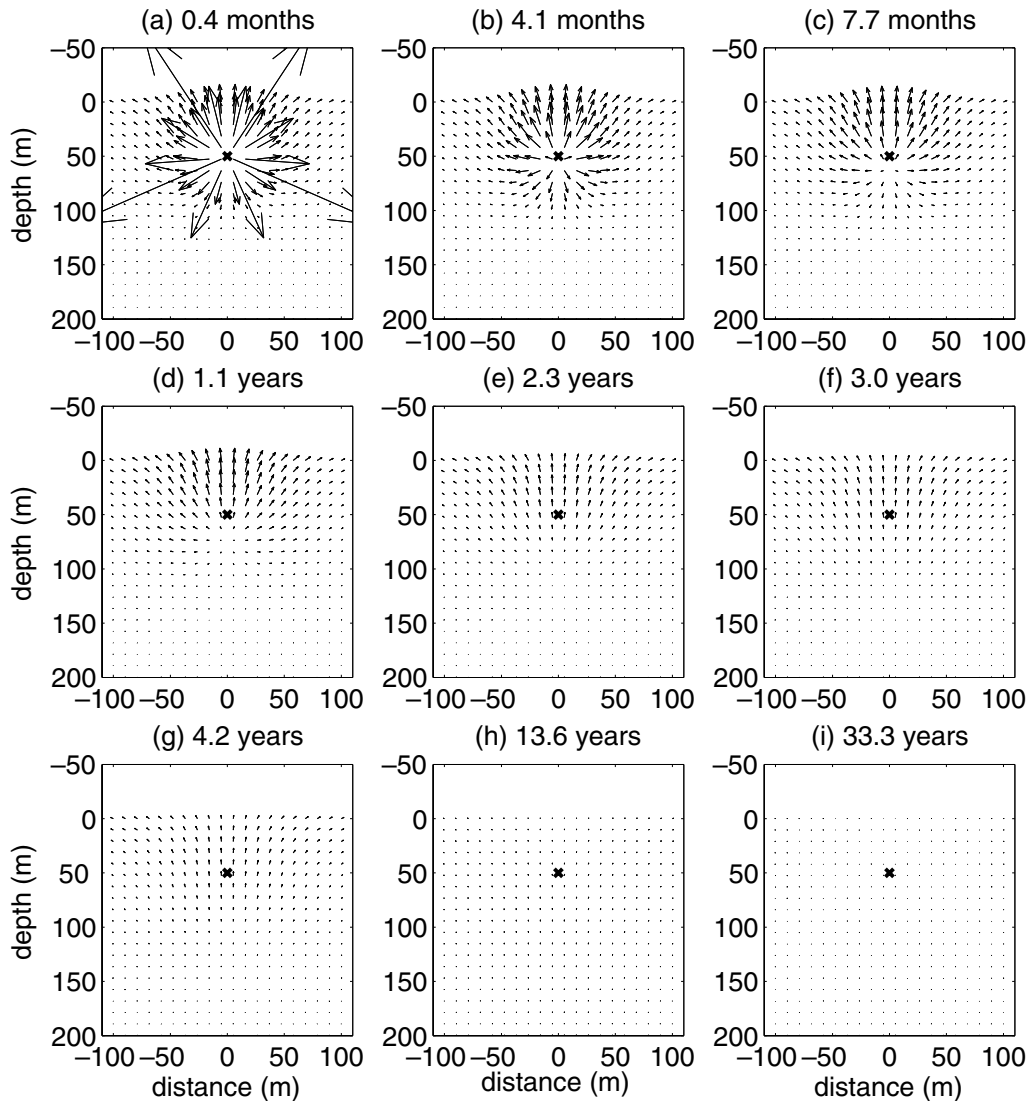


Figure 2. Temporal evolution of the displacement field due to a point heat source of $q = 5 \times 10^9 \text{ m}^3 \text{ K}$ at a depth of 50 m. The vertical cross-section passing through the point heat source is shown. The scale of the displacement vector is the same as the horizontal and vertical axes.

the instantaneous heat source is assumed to be $5 \times 10^9 \text{ m}^3 \text{ K}$, since a typical volume change due to volcanic eruptions is $5 \times 10^6 \text{ m}^3$ and the temperature of magma is 10^3 K . Other material parameters are assumed as $\kappa = 10^{-5} \text{ m}^2 \text{ s}^{-1}$, $\alpha = 2 \times 10^{-5}$ and $\nu = 0.3$. For simplicity, we ignore a melting of the ambient country rock due to the intruded high-temperature magma, and hence do not account for the effect of viscoelasticity and associated relaxation processes suggested by Newman *et al.* (2001); the viscoelastic model of Newman *et al.* (2001), however, does not generate a heat flow on the surface, while the thermoelastic model will obviously do this. Moreover, because of the latent heat of fusion, magma releases additional heat other than the intrinsic heat, which will retard the cooling of country rock. If we assume the magma density and latent heat of fusion as 3000 kg m^{-3} and 320 kJ kg^{-1} , respectively (Turcotte & Schubert 2002), the latent heat in the above case is $4.8 \times 10^{15} \text{ J}$. However, the corresponding heat for the entire magma with a temperature of 10^3 K and a specific heat of $1.2 \text{ kJ kg}^{-1} \text{ K}^{-1}$ can be estimated to be $3000 \times 1200 \times 5 \times 10^6 \times 10^3 = 1.8 \times 10^{16} \text{ J}$, which is a factor of four greater than the latent heat. Hereafter, we will also ignore the effect of latent heat release associated with solidification.

We may interpret the temporal evolution in Fig. 2 as follows. The instantaneous heat source causes a co-intrusive thermoelastic deformation not only around the source but also on the surface, since the source generates an instantaneous thermal stress. The largest deformation takes place in the vicinity of the heat source, but the large displacements near the source in Fig. 2(a) are physically unrealistic; we will discuss this apparent inconsistency in the next paragraph. The heat source region immediately starts to cool via thermal diffusion and contract through thermoelasticity. As time elapses, the displacement around the heat source is no longer the greatest (Figs 2b–i), whereas the displacements on the surface will last for a somewhat longer time (see also Fig. 5). Namely, the closer to the heat source, the earlier the transient displacements will start compared with those close to the surface (see Fig. 5). The temperature in the ambient region will temporarily increase as the heat diffuses away from the source region, which contributes to a continuous expansion. The effect of this temporal increase in temperature upon displacement is, however, much smaller than that of the initially assigned temperature change at the source, and thus the temporal expansion

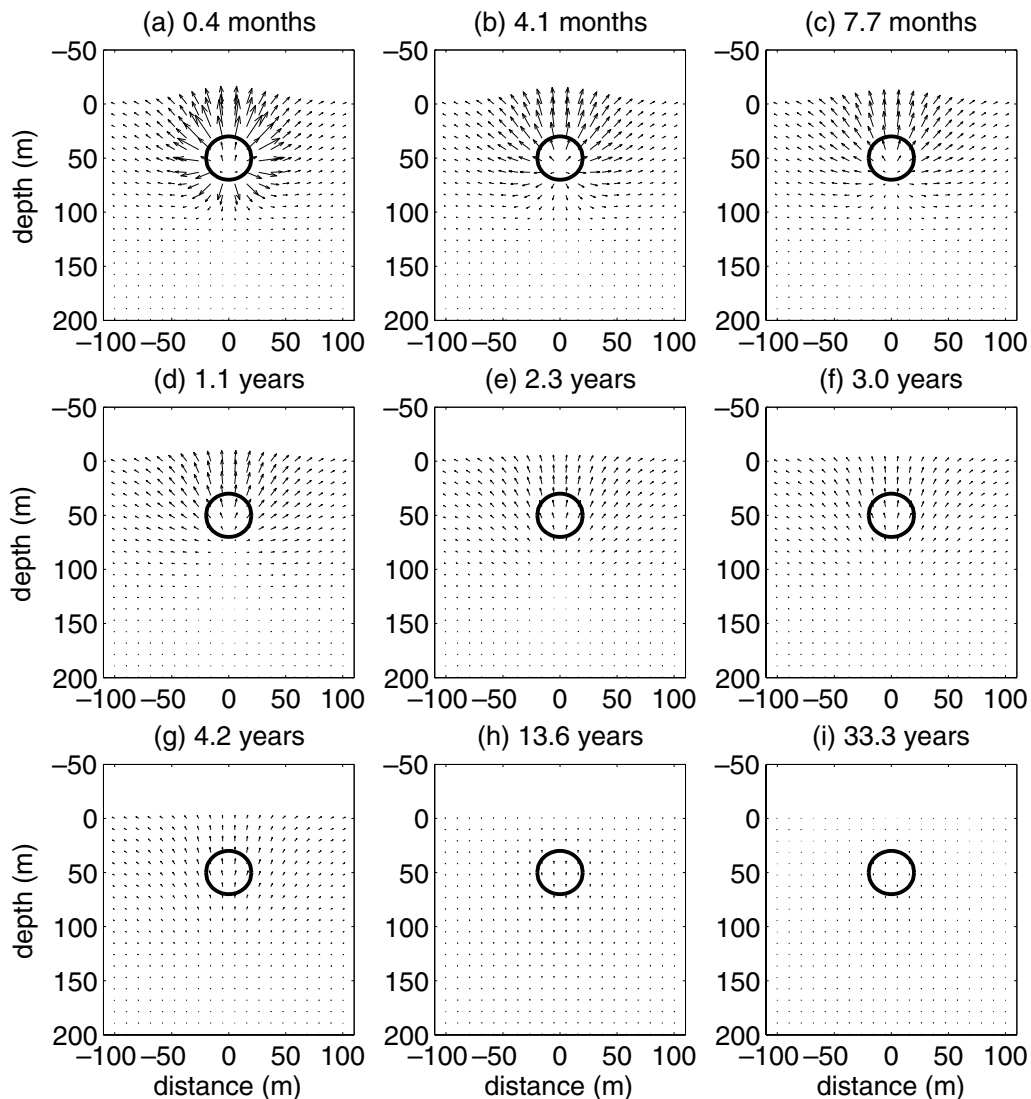


Figure 3. Temporal evolution of the displacement field due to a spherical shell heat source of $q = 5 \times 10^9 \text{ m}^3 \text{ K}$ at a depth $d = 50 \text{ m}$: the radius is $a = 20 \text{ m}$. The vertical cross-section passing through the heat source is shown. The scale of the displacement vector is the same as the horizontal and vertical axes.

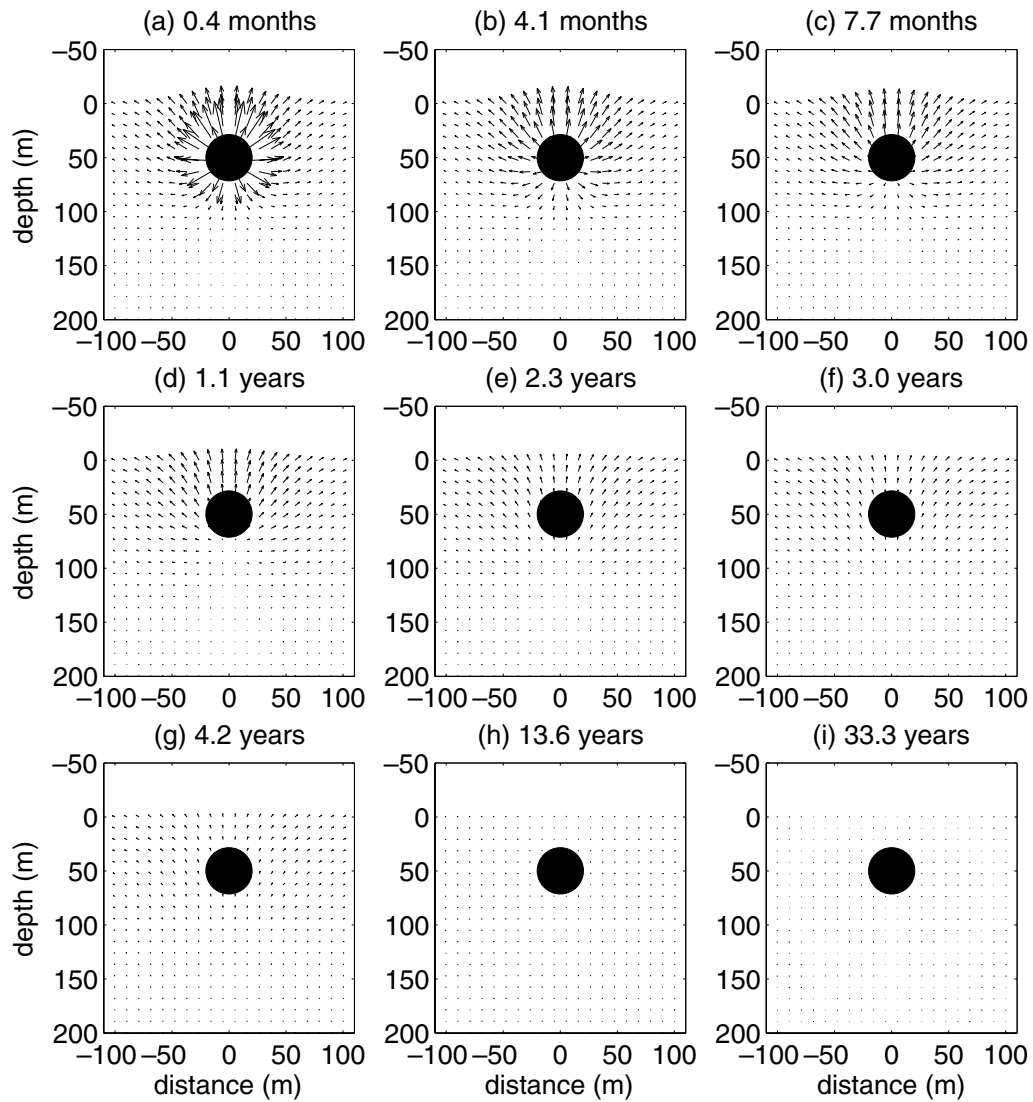


Figure 4. Temporal evolution of the displacement field due to a spherical volume heat source of $q = 5 \times 10^9 \text{ m}^3 \text{ K}$ at a depth $d = 50 \text{ m}$: radius $a = 20 \text{ m}$. The vertical cross-section passing through the heat source is shown. The scale of the displacement vector is the same as the horizontal and vertical axes.

is negligible in comparison with the co-intrusive expansion. As time goes by, the temperature will start to decrease and thus gradually contract in the ambient region as well. Measurable post-intrusive transient deformation on the surface starts about 1 month after the intrusion of the heat source (see Fig. 5). The duration of the co-intrusive displacement and the initiation of transient displacement will henceforward depend on how long the elastic thermal contraction takes to reach the observation point from the source region. For heat to diffuse a distance d would take a time t of the order of $d^2/4\pi\kappa$. In the present case of $d = 50 \text{ m}$ with $\kappa = 10^{-5} \text{ m}^2 \text{ s}^{-1}$, this can be estimated to be 0.76 months, which we confirmed numerically. Indeed, Fig. 5 illustrates that the region closer to the heat source starts to cool down earlier than the more distant region. How long, then, will the thermoelastic displacement take to settle down completely? Since it would be the time when the initial heat magnitude Q can diffuse entirely away, we can evaluate it as $Q^{2/3}/4\pi\kappa$. In the present case, this is about 74 yr, which we again confirmed numerically (Fig 5). In reality, however, the final stage of settling down is a very slow process, and the most rapid transient deformation can take place for decades after the inclusion of the heat source.

Fig. 2(a) shows that the displacement amplitude exceeds the source depth. This anomaly would be partly due to a fundamental assumption in the thermal diffusion equation for the instantaneous heat source, which hypothesizes that heat flow is simply proportional to the spatial gradient in temperature (Fourier's law), and partly due to the largest heat source density associated with the 'point' source. Fourier's law would be valid and well-accepted for stationary and time-independent heat conduction problems. However, we should note that Fourier's law when applied to a transient problem such as an instantaneous source generates an infinitely large temperature gradient and thus a heat flux even at places much further away from the source region at the instant of the source inclusion. This is obviously unrealistic, and in a strict sense it is physically inconsistent to apply Fourier's law to time-dependent problems (e.g. Morse & Feshbach 1953, p. 865). We think that this unphysical situation becomes particularly evident in the case of a point source, which will generate an unrealistically large temperature increase near the source. However, Fourier's law will provide an approximate heat flow if time elapses sufficiently, and is mathematically easy to deal with,

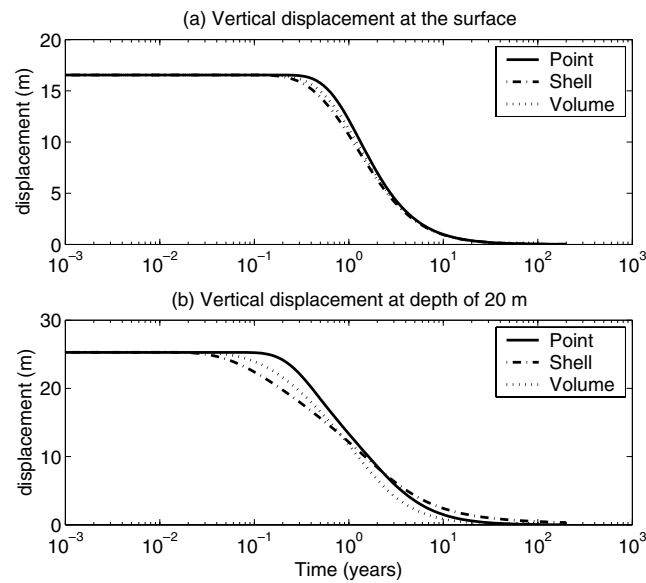


Figure 5. Temporal evolution of a vertical displacement observed (a) at the surface and (b) at depth $d = 20$ m as a function of elapsed time (yr) after the intrusion of the heat source; note that the horizontal axis is in a logarithmic scale. Solid, dash-dotted and dotted lines stand for point, spherical shell and spherical volume sources, respectively. The total heat source $q = 5 \times 10^9 \text{ m}^3 \text{ K}$ is instantaneously set at a depth $d = 50$ m; the spherical radius $a = 20$ m.

providing us with a perspective on the transient diffusion problems in hand. Thus, Fourier's law has been applied even to transient problems in a wide range of disciplines (Carslaw & Jaeger 1959; Nowacki 1962).

3.2 Comparison between a point source and spherical sources

For a comparison with the point heat source response, we show numerical results of heat sources with both a spherical shell (Fig. 3) and a spherical volume (Fig. 4). The initial amount of heat is the same as in the point source, but the spherical radius is set to be 20 m. Also shown in Fig. 5 is a comparison of the transient vertical displacements observed at the surface and at a depth of 50 m; the horizontal location is the same as the source.

The most significant difference is seen in the vicinity of the heat source at the first stage (Figs 2a, 3a and 4a). This is obviously due to differences in the heat source density, which is largest for the point heat source. In the far field, however, we do not recognize any differences in the co-intrusive displacements for any of the three sources (Fig. 5). Namely, a far-field solution is dependent on the total heat magnitude, and the point source thus provides a reasonable approximation, although how far we will observe the deformation depends on the magnitude of the heat source.

Fig. 5(b) shows that the shell heat source is fastest to initiate a transient deformation, but is slowest to settle down. The rapid initiation of transient deformation occurs because the shell source can most efficiently release heat towards both the inside and outside of the source region. Meanwhile, the slow termination occurs because the heat flowing into the shell must ultimately escape from the shell, which takes longest in comparison with the other sources.

Although the evolution of both point and spherical volume sources looks roughly similar (Fig. 5), the initiation of transient deformation is faster for the spherical volume source. This is due to a broad distribution of heat sources allowing heat to be released more efficiently.

4 APPLICATION TO INSAR OBSERVATION OF POST-ERUPTIVE DEFORMATION

4.1 The 1986 eruption of the Izu-Oshima volcano, Japan

The Izu-Oshima volcano is a basaltic stratovolcano island on the northern edge of the Philippine Sea Plate, about 100 km south-southwest of Tokyo, Japan (Fig. 6). Recent eruptive activity extends back to 1986 November. On 1986 November 21 the lava flows and scoria cone were generated by a fissure eruption that began on the caldera floor at the northeastern foot of Mount Mihara (Fig. 7); Mount Mihara is also a scoria cone due to the great 1777 eruptions. It has summit pit crater (A in Fig. 7) and the difference in elevation exceeds 150 m above the caldera floor. Fig. 7 shows the spatial distribution of recent lava and scoria cone, redrawn from Isshiki (1984) and Kawanabe (1998). The height of the scoria cone relative to the caldera floor and the lava thickness due to the 1986 eruptions were measured by photogrammetry (Nagaoka 1988). The maximal difference in elevation at cone B (CB) was 45 m at the north of crater B (Fig. 7). The thickness of lava emplaced upon the caldera floor is, on average, 5–7 m for LB1, 10–20 m for LB3 and 4–5 m for LA (Fig. 7). While the volume of the 1950–1951 and 1986

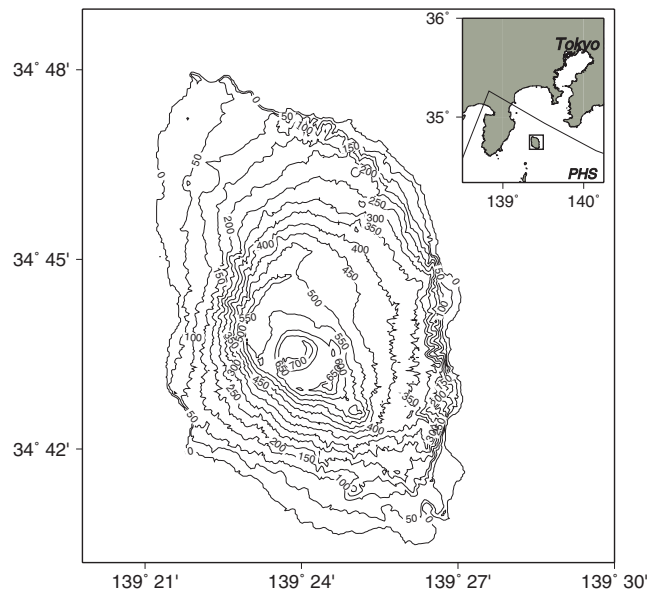


Figure 6. Location and elevation map of Izu-Oshima volcano island, Japan. PHS stands for Philippine Sea Plate.

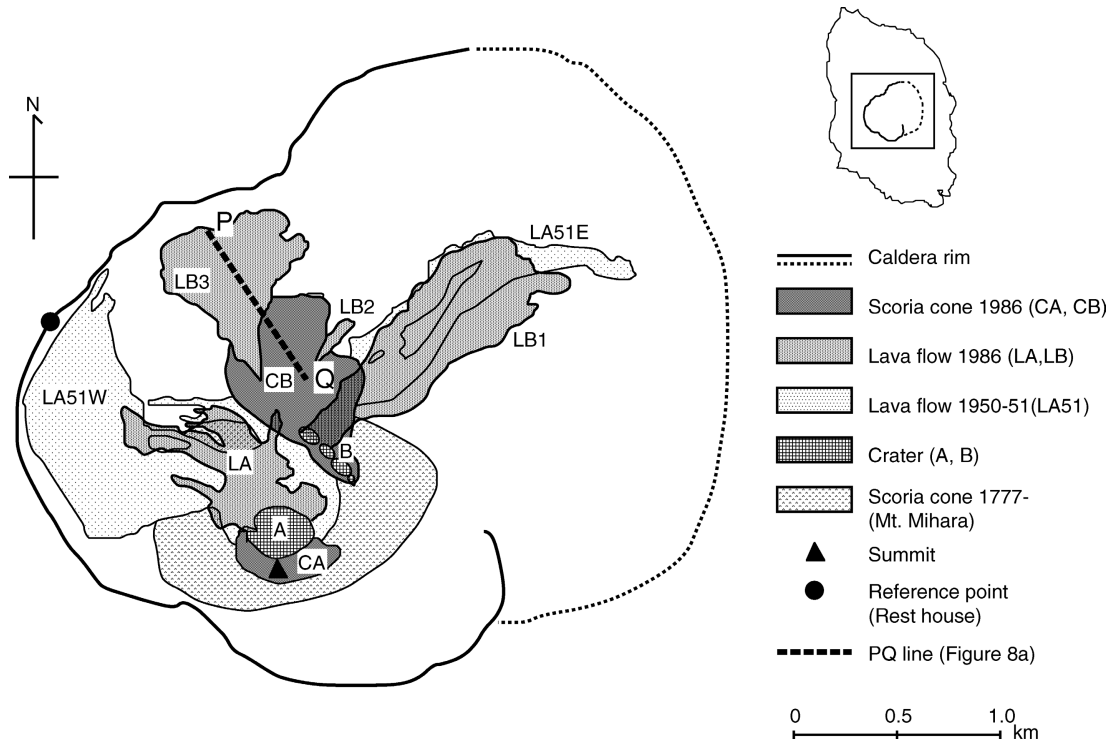


Figure 7. Distribution of the crater, lava and scoria cone inside the caldera by the 1950–1951 and 1986 eruptions, redrawn from Isshiki (1984) and Kawanabe (1998). The crater B was first formed during the 1986 eruptions. LA (CB) stands for the lava (cone) from the crater A (B). The 1986 LB1 flowed out upon the 1951 LA51E, whose shape is explicitly shown. Note that some area in the middle part of LA51E was left unchanged.

lava is estimated to be $2.3 \times 10^7 \text{ m}^3$ and $1.9 \times 10^7 \text{ m}^3$, the volume of scoria due to the 1950–1951 and 1986 eruptions is $0.36 \times 10^7 \text{ m}^3$ and $1.73 \times 10^7 \text{ m}^3$, respectively (Sakaguchi *et al.* 1987).

In the early 1990s, it was confirmed through precise crustal deformation measurements by EDM (electro-optic distance measurement) and GPS (Global Positioning System) that the ground surface was exhibiting tumescence. The swelling has been explained as due to an inflation source (Mogi 1958), and has been interpreted as representing a refilling of the deeper magma chamber with new magma at a depth of around 8–10 km, indicating the possibility of future eruptions (Watanabe 1995). Nevertheless, as already shown by InSAR data from the Japanese Earth Resource Satellite (JERS) (Murakami *et al.* 1998; Okuyama *et al.* 2002), we can observe a localized deformation around the

Table 1. ERS1/2 Data in this study and maximum subsidence rate.

Pair	Date (ERS1/ERS2)	Time span (yr)	B_{\perp}/H_a (m)	Subsidence rate (cm yr ⁻¹)
a	1995 Oct. 1/1997 Sept 1	1.92	10.2/124.5	3.3 ± 0.7
b	1993 May 21/1998 Nov. 30	5.53	5.1/249.0	3.1 ± 0.7
c	1993 July 30/1999 June 28	5.91	15.2/83.6	3.1 ± 0.7
d	1993 Apr. 16/1999 Apr. 19	6.01	3.6/352.8	2.7 ± 0.9

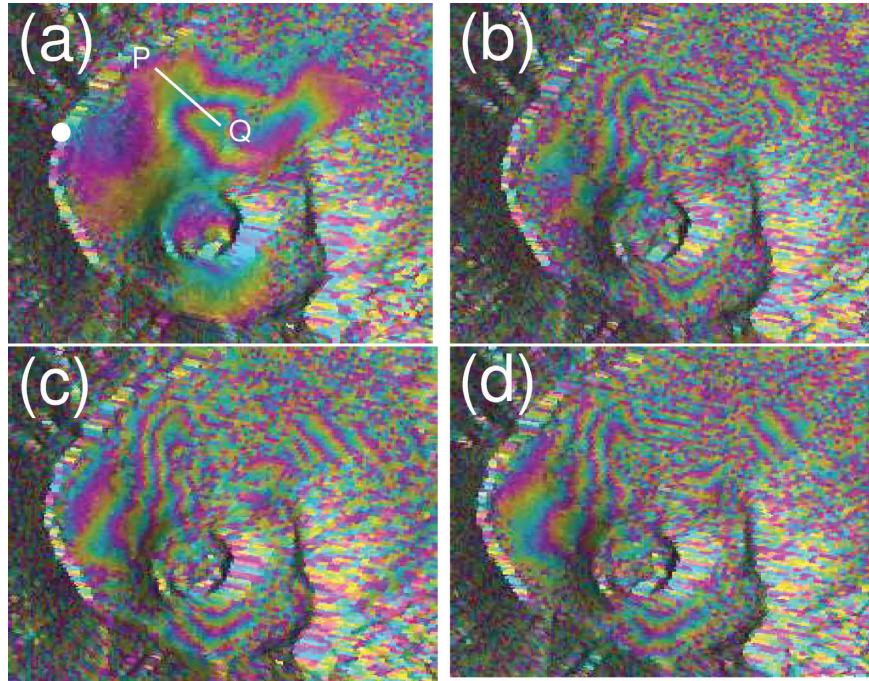


Figure 8. Four differential interferograms around the caldera; see Table 1 for each measurement period and perpendicular baseline. Phase values of interferogram are wrapped, and one colour cycle corresponds to a line of sight change of 2.8 cm, half the wavelength of the ERS1/2 data. The deformation rate profile along P–Q in (a) with respect to the reference (white circle) is shown in Fig 9.

caldera through European Remote Sensing satellite (ERS1/2) InSAR data, which we will account for using the thermoelastic theory derived in the preceding sections.

4.2 InSAR data and analysis result

InSAR is a remote sensing technique that is capable of detecting ground displacements of the order of millimetres to centimetres through differential measurements of the phase component of temporally separated SAR signals (e.g. Massonnet & Feigl 1998; Hanssen 2001).

Four interferograms derived from ERS1/2 SAR images between 1995 and 1999 were used for analysis (Table 1). InSAR analysis can be easily accomplished where coherence loss is small. The area covered with lava flow preserves a high coherence (Lu & Freymuller 1998). Also, only data pairs with perpendicular baseline components (baseline component projected perpendicular to the viewing direction) of less than 20 m were used in this study (Table 1) so as to avoid spatial decorrelation as well as to minimize the sensitivity of the phase measurement to topographic roughness. The height ambiguity H_a in Table 1 is the topographic height difference causing one cycle of phase change. As the topographic variation in the caldera is less than 250 m, the short perpendicular baseline pairs allow us to suppress errors in the 50 m mesh digital elevation model (DEM) derived by the Geographical Survey Institute (GSI). Hence, the detected fringes in Fig. 8 are entirely due to ground displacements.

Differential interferograms in Fig. 8 show that the area of largest displacement closely matches CB and LB3 in Fig. 7. Moreover, the deformation rate along P–Q in Fig. 8(a) is largely proportional to the relative height of the CB (Fig. 9); the errors in the estimated deformation rate and deposit thickness are ± 0.6 cm yr⁻¹ and ± 5 m, respectively. Note that the data pairs in Fig. 8 were acquired about 7–9 yr after the 1986 eruption. Fig. 8(a) tells us that the maximal change in the line-of-sight at a point Q with respect to the reference point is 5.9 ± 1.2 cm; uncertainties are largely due to those at the reference point. If we suppose a source beneath Q, the displacement at that point can be regarded as entirely due to the vertical component. With a nominal angle of $23 \pm 3^\circ$ for the look angle, we can convert the line-of-sight changes to the vertical displacements by multiplying by 1.064. Thus, the subsidence rate at Q is 3.3 cm yr⁻¹. The estimated subsidence rates at that point for other data pairs are also shown in Table 1.

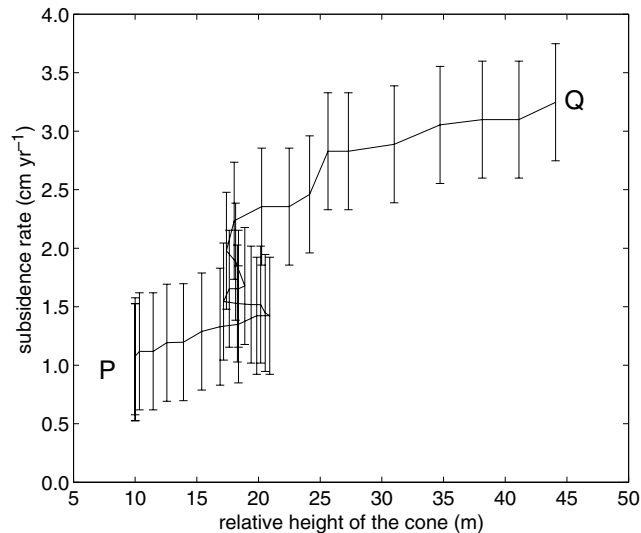


Figure 9. Estimated subsidence rate profile as a function of the relative height of cone B along the line P–Q in Fig. 8(a). The reference point of the subsidence is at the circle in Fig. 8(a).

4.3 Modelling cone formation and subsequent secular ground displacement

4.3.1 Result

Assuming that the newly formed cone and subsequent secular ground displacement are caused by magma intrusion at very shallow depth and subsequent thermoelastic contraction, to what extent can we explain the observed size of the cone and post-eruptive deformation? To this end, we use both the Mogi model to represent a static mass intrusion and the formulation for a quasi-static thermoelastic deformation derived in the preceding section. As shown by McTigue (1987), Mogi's 'point' inflation model can be used, to a good approximation, as a spherical finite volume source even when its radius to depth ratio exceeds 0.5. Meanwhile, since temporal evolution of the post-eruptive deformation depends upon whether a point or a spherical volume source is assumed, we will employ the formulation for a spherical volume source. Although we use the term 'co- and post-eruptive' deformation, what the proposed thermoelastic formulations can compute is actually a 'co- and post-intrusive' deformation, since they do not deal with any eruption processes themselves. Thus the derived source parameters below should be regarded as caused by an equivalent intrusion source.

As shown by Delaney & McTigue (1994), the injection volume is two-thirds of the uplift volume if they are caused by a spherical volume source with Poisson's ratio 0.25. With reference to the estimate by Sakaguchi *et al.* (1987), we see that the injected volume is $1.15 \times 10^7 \text{ m}^3$, and that its radius is 140 m.

Figs 10(a) and (b) indicate the predicted co-eruptive displacement fields on the surface due to the Mogi source and those due to the thermoelastic effect, respectively. For the computation, we assumed a central depth of the source at 240 m, a temperature step of 10^3 K , a thermal diffusivity of $10^{-5} \text{ m}^2 \text{ s}^{-1}$ and a linear thermal expansivity of 2×10^{-5} . These material properties are largely consistent with laboratory-derived values, although the thermal diffusivity is appreciably larger by a factor of 10 (e.g. Turcotte & Schubert 2002). We speculate that since the actual cooling process involves not only a pure thermal diffusion but also a forced cooling by meteorological and/or ground water factors, as well as a convective process due to a vesiculation of volatiles, magma can be cooled down more efficiently, and that thermal diffusivity can be effectively higher than a laboratory-derived value. The total annual precipitation at Izu-Oshima is 2000–3000 mm on average (Japan Meteorological Agency, <http://www.data.kishou.go.jp>).

Comparing Figs 10(a) and (b), the co-eruptive displacement due to the mass intrusion is an order of magnitude greater than that due to the thermoelastic expansion effect. However, the Mogi source has no contribution to the post-eruptive transient deformation, and the thermoelastic effect alone can generate the post-eruptive deformation. Figs 10(c) and (d) show snapshots of the thermoelastic displacement fields on the surface at the instant of 18.3 yr and 50.7 yr after intrusion of the heat source, respectively. Although the displacement amplitudes are smaller than those due to co-eruptive deformation, those predicted changes are measurable by current geodetic techniques. Figs 10(e) and (f) show temporal changes in vertical ground displacement and subsidence rate at a ground surface immediately above the source. In Fig. 10(f), observed subsidence rates are indicated. Both the amplitude of maximum uplift and the horizontal coverage of co-eruptive displacement in Fig. 10 are consistent with cone B at the time of the 1986 fissure eruption (see Figs 7 and 9). The observed post-eruptive subsidence rate is also in good agreement with the prediction. It is interesting to note from Fig. 10(f) that the maximum subsidence rate will occur more than two decades after the intrusion of the heat source.

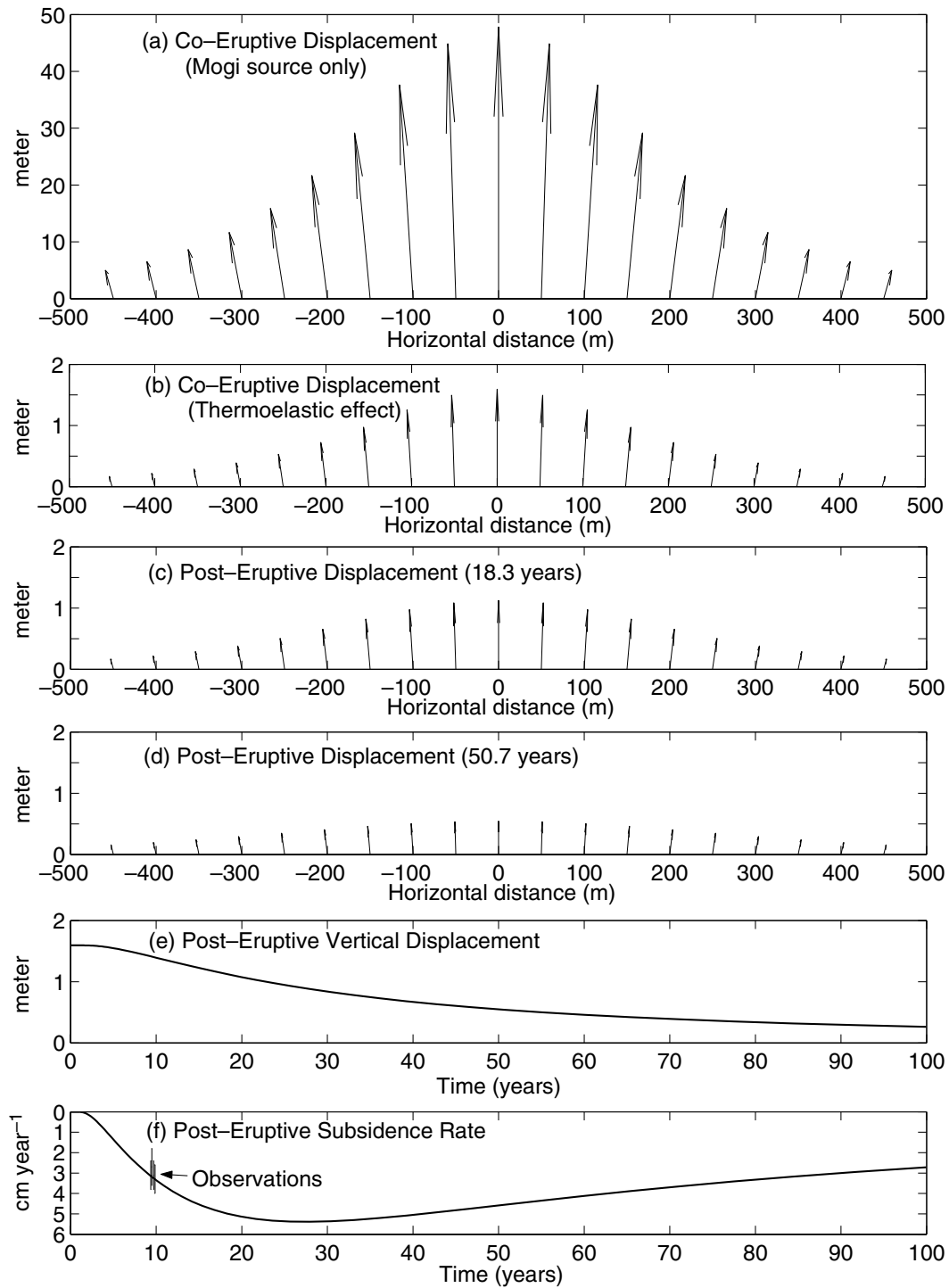


Figure 10. Spatial and temporal changes of co-eruptive and post-eruptive displacement fields at the surface due to an equivalent intrusive source; see text for prescribed parameters. (a) Co-eruptive displacements due to mass intrusion as a function of horizontal scale. (b) Co-eruptive displacements due only to the thermoelastic effect. (c, d) Post-eruptive displacement at the instant of (c) 18.3 yr and (d) 50.7 yr after intrusion of the heat source. (e) Co- and post-eruptive vertical displacement at the surface immediately above the heat source as a function of time (yr) after the intrusion. (f) Post-eruptive subsidence rate at the surface immediately above the heat source as a function of time (yr) after the intrusion. Four observed rates of subsidence in Table 1 are shown together.

4.3.2 Discussion

These results suggest that further extensive ground surface measurements can better constrain the heat sources in the previous eruptions. The results also have an implication for prediction of eruptions based upon precision measurement of ground movement. Namely, in order to assess the ground displacement data for a forthcoming eruption event, we need to accurately evaluate the effect of previous eruptive activities upon the on-going ground displacement.

We have assumed so far that the observed post-eruptive deformation was caused by thermoelastic contraction of the magma intruded at a shallow depth. Consolidation of the substrate due to the deposited load is another possible subsidence mechanism. Employing Terzaghi's consolidation theory (e.g. Wang 2000), we can roughly evaluate the plausibility of a consolidation mechanism. The characteristic time T for consolidation is estimated by hydraulic diffusivity c (consolidation coefficient) and the thickness of the substrate z :

$$T \sim \frac{z^2}{4c}. \quad (18)$$

In order for that process to last longer than a decade with a thickness of the order of 10^3 m, the maximal allowable hydraulic diffusivity is $10^{-3} \text{ m}^2 \text{ s}^{-1}$; if the substrate is thinner, a smaller hydraulic diffusivity is required. In the case of granite, the permeability of which can be as low as 10^{-18} m^2 , the hydraulic diffusivity is of the order of 10^{-4} – $10^{-5} \text{ m}^2 \text{ s}^{-1}$ (Wang 2000). However, the actual substrate would be porous basaltic lava and scoria deposits, and indeed the horizontal permeability at Izu-Oshima has been estimated to be as high as 10^{-8} m^2 (Koizumi *et al.* 1998), based upon water well observation data. This value is orders of magnitude greater than that for sand or sandstone, whose permeability and hydraulic diffusivity are 10^{-12} m^2 and 10^{-1} – $1 \text{ m}^2 \text{ s}^{-1}$ (Wang 2000, Table 3.1). Hence, the consolidation process, if any, should be much faster, and would not last longer than a decade, although crude estimates based on a 1-D theory cannot totally rule out the possibility of such a mechanism.

5 CONCLUSION

We have derived closed analytical solutions for a quasi-static thermoelastic deformation response to instantaneous point and spherical heat sources in an elastic half-space, and examined the spatiotemporal displacement fields. We generated differential interferograms at Izu-Oshima volcano, Japan, using ERS1/2 data, and interpreted the post-1986 eruption deformation by applying the derived solutions for a quasi-static thermoelastic deformation. Using realistic parameter values of physical properties, we were able to obtain a good agreement between observation and calculation. A copy of the MATLAB codes (MATLAB is a registered trademark of The MathWorks, Inc., Natick, MA, USA; <http://www.mathworks.com/>) can be obtained from the author upon request.

ACKNOWLEDGMENTS

The author expresses sincere thanks to S. Okubo for his continuous support for the author's SAR studies. Also, the author thanks J. H. Davies for discussing the derivation of quasi-static solution and J. M. Wahr for comments and discussion. This work was partly carried out at the University of Colorado at Boulder as a visiting faculty member supported by MEXT, Japan as well as CIRES, University of Colorado, and partly supported by Grant-in-Aid for Encouragement of Young Scientists (B), MEXT, Japan. Comments from E. Rivalta and R. Bürgmann are gratefully acknowledged. ERS1/2 data are courtesy of the European Space Agency. The former NASDA, currently named JAXA, received the ERS1/2 data.

REFERENCES

- Abramowitz, M. & Stegun, I.A. (eds), 1972. *Handbook of Mathematical Functions with Formulas, Graphs, and Mathematical Tables*, Dover, New York.
- Briole, P., Massonnet, D. & Delacourt, C., 1997. Post-eruptive deformation associated with the 1986–87 and 1989 lava flows of Etna detected by radar interferometry, *Geophys. Res. Lett.*, **24**(1), 37–40, doi:10.1029/96GL03705.
- Carlsaw, H.S. & Jaeger, J.C., 1959. *Conduction of Heat in Solids*, 2nd edn, Oxford University Press, London.
- Davies, J.H., 2003. Elastic field in a semi-infinite solid due to thermal expansion or a coherently misfitting inclusion, *ASME J. Appl. Mech.*, **70**, 655–660.
- Delaney, P.F. & McTigue, D.F., 1994. Volume of magma accumulation or withdrawal estimated from surface uplift or subsidence, with application to the 1960 collapse of Kilauea volcano, *Bull. Volcanol.*, **56**, 417–424.
- Fialko, Y. & Simons, M., 2000. Deformation and seismicity in the Coso geothermal area, Inyo County, California: observations and modeling using satellite radar interferometry, *J. geophys. Res.*, **105**(B9), 21 781–21 794, doi:10.1029/2000JB900169.
- Furuya, M., 2004. Localized deformation at Miyakejima volcano based on JERS-1 radar interferometry: 1992–1998, *Geophys. Res. Lett.*, **31**, L05605, doi:10.1029/2003GL019364.
- Hanssen, R.F., 2001. *Radar Interferometry—Data Interpretation and Error Analysis*, Kluwer Academic, Dordrecht.
- Isshiki, N., 1984. *Geology of the Oshima District*, (in Japanese with English abstract), Quadrangle Series, scale 1:50 000, Geological Survey of Japan.
- Kawanabe, Y., 1998. *Geological Map of the Izu-Oshima Volcano*, (in Japanese with English abstract), Geological Map of Volcanoes 10, scale 1:25 000, Geological Survey of Japan.
- Koizumi, N., Kitagawa, Y., Kazahaya, K. & Tahakashi, M., 1998. Volcanic gas concentration and aquifer permeability estimated from tidal fluctuations in ground water level: case of Koshimizu Well in Izu-Oshima, Japan, *Geophys. Res. Lett.*, **25**(12), 2237–2240, doi:10.1029/98GL01409.
- Lu, Z. & Freymuller, J., 1998. Synthetic aperture radar interferometry coherence analysis over Katmai volcano group, Alaska, *J. geophys. Res.*, **103**, 29 887–29 894, doi:10.1029/98JB02410.
- Massonnet, D. & Feigl, K.L., 1998. Radar interferometry and its application to changes in the Earth's surface, *Rev. Geophys.*, **36**, 441–500.
- Masterlark, T. & Lu, Z., 2004. Transient volcano deformation sources imaged with interferometric synthetic aperture radar: application to Seguam Island, Alaska, *J. geophys. Res.*, **109**, B01401, doi:10.1029/2003JB002568.
- McTigue, D.F., 1987. Elastic stress and deformation near a finite spherical magma body: resolution of the point source paradox, *J. geophys. Res.*, **92**(B12), 12 931–12 940.
- Mindlin, R.D. & Cheng, D.H., 1950a. Nuclei of strain in the semi-infinite solid, *J. Appl. Phys.*, **21**, 926–930.
- Mindlin, R.D. & Cheng, D.H., 1950b. Thermoelastic stress in the semi-infinite solid, *J. Appl. Phys.*, **21**, 931–933.
- Mogi, K., 1958. Relations between the eruptions of various volcanoes and deformations of the ground surfaces around them, *Bull. Earthq. Res. Inst. Univ. Tokyo*, **36**, 99–134.

Morse, P.M. & Feshbach, H., 1953. *Methods of Theoretical Physics I*, McGraw-Hill, New York.

Murakami, M., Fujiwara, S., Nakagawa, H., Tobita, M. & Rosen, P., 1998. Crustal deformation of Izu-Oshima Detected by JERS-1 Interferometric SAR (abstract in Japanese), paper presented at *90th Fall Meeting of The Geodetic Society of Japan, Kyoto, Japan*, 102.

Nagaoka, M., 1988. Geomorphological characteristics of volcanic products of the 1986 eruption of Izu-Oshima volcano and its volume measured by photogrammetry (in Japanese with abstract and figure captions in English), *Bull. Volcanol. Soc. Japan, Ser. 2*, **33**, S7–S15.

Newman, A.V., Dixon, T.H., Ofoegbu, G.I. & Dixon, J.E., 2001. Geodetic and seismic constraints on recent activity at Long Valley Caldera, California: evidence for viscoelastic rheology, *J. Volc. Geotherm. Res.*, **105**, 183–206.

Nowacki, W., 1962. *Thermoelasticity*, Polish Scientific Publishers, Warsaw.

Okuyama, S., Takemoto, S., Murakami, M., Tobita, M., Fujiwara, S.,

Nakagawa, H. & Yurai, H., 2002. Localized crustal deformation in Izu-Oshima island derived from D-InSAR (in Japanese), *Chikyu Monthly, Special Issue*, **33**, 90–95.

Sakaguchi, K., Okumura, K., Soya, T. & Ono, K., 1987. *The 1986 Eruption of Izu-Oshima Volcano*, (in Japanese with English abstract), Miscellaneous Map Series 26, scale 1:25 000, Geological Survey of Japan.

Stevens, N., Wadge, G., Williams, C.A., Morley, J.G., Muller, J.-P., Murray, J.B. & Upton, M., 2001. Surface movements of emplaced lava flows measured by synthetic aperture radar interferometry, *J. geophys. Res.*, **106**(B6), 11 293–11 313, doi:10.1029/2000JB900425.

Turcotte, D. & Schubert, G., 2002. *Geodynamics*, 2nd edn, Cambridge University Press, New York.

Wang, H.F., 2000. *Theory of Linear Poroelasticity with Applications to Geomechanics and Hydrogeology*, Princeton University Press, Princeton.

Watanabe, H., 1995. Magma is storing again beneath Izu-Oshima volcano (in Japanese), *Kagaku*, **65**, 631–633.

APPENDIX A:

The derivation of $\Phi_{ss}^{(\infty)}$ is shown below:

$$\Phi_{ss}^{(\infty)} = -\frac{m}{4\pi} \int \int \frac{\eta a \sin \psi d\lambda d\psi}{\sqrt{R^2 + a^2 - 2Ra \cos \psi}} \operatorname{erf}\left(\frac{\sqrt{R^2 + a^2 - 2Ra \cos \psi}}{\sqrt{\theta}}\right), \quad (\text{A1})$$

$$= -\frac{2\pi \eta a^2 m}{4\pi} \int_0^\pi \frac{\sin \psi d\psi}{\sqrt{R^2 + a^2 - 2Ra \cos \psi}} \operatorname{erf}\left(\frac{\sqrt{R^2 + a^2 - 2Ra \cos \psi}}{\sqrt{\theta}}\right), \quad (\text{A2})$$

$$= -\frac{2\pi \eta a^2 m}{4\pi} \int_{-1}^1 \frac{ds}{\sqrt{R^2 + a^2 + 2Ras}} \operatorname{erf}\left(\frac{\sqrt{R^2 + a^2 + 2Ras}}{\sqrt{\theta}}\right), \quad (\text{A3})$$

$$= -\frac{\eta a m \sqrt{\theta}}{2R} \int_{|R-a|/\sqrt{\theta}}^{(R+a)/\sqrt{\theta}} \operatorname{erf} X dX, \quad (\text{A4})$$

$$= -\frac{\eta a m \sqrt{\theta}}{2R} [X + \operatorname{ierfc}(X)]_{|R-a|/\sqrt{\theta}}^{(R+a)/\sqrt{\theta}}. \quad (\text{A5})$$

APPENDIX B:

The following integration formula is necessary in the derivation of eq. (21):

$$\int_{x_0}^{x_1} y \operatorname{ierfc}(y) dy = \left[\frac{y^2}{2} \operatorname{ierfc}(y) \right]_{x_0}^{x_1} + \int_{x_0}^{x_1} \frac{y^2}{2} \operatorname{erfc}(y) dy, \quad (\text{B1})$$

$$= \left[\frac{y^2}{2} \operatorname{ierfc}(y) + \frac{y^3}{6} \operatorname{erfc}(y) \right]_{x_0}^{x_1} + \frac{1}{3\sqrt{\pi}} \int_{x_0}^{x_1} y^3 \exp(-y^2) dy, \quad (\text{B2})$$

$$= \left[\frac{y^2}{2} \operatorname{ierfc}(y) + \frac{y^3}{6} \operatorname{erfc}(y) - \frac{1}{6\sqrt{\pi}} (y^2 + 1) \exp(-y^2) \right]_{x_0}^{x_1}. \quad (\text{B3})$$